# RESEARCH ARTICLE

# Dual Topology of Dirac Electron Transport and Photogalvanic Effect in Low-Dimensional Topological Insulator Superlattices

*Hao-pu Xue, Rui Sun, Xu Yang, Andrew Comstock, Yangrui Liu, Binghui Ge, Jia-nan Liu, Yan-sheng Wei, Qing-lin Yang, Xue-song Gai, Zi-zhao Gong, Zong-kai Xie, Na Li, Dali Sun,\* Xiang-qun Zhang, Wei He, and Zhao-hua Cheng\**

Dual topological insulators, simultaneously protected by time-reversal symmetry and crystalline symmetry, open great opportunities to explore different symmetry-protected metallic surface states. However, the conventional dual topological states located on different facets hinder integration into planar opto-electronic/spintronic devices. Here, dual topological superlattices (TSLs) $Bi_2Se_3$-$(Bi_2/Bi_2Se_3)_N$ with limited stacking layer number $N$ are constructed. Angle-resolved photoelectron emission spectra of the TSLs identify the coexistence and adjustment of dual topological surface states on $Bi_2Se_3$ facet. The existence and tunability of spin-polarized dual-topological bands with $N$ on $Bi_2Se_3$ facet result in an unconventionally weak antilocalization effect (WAL) with variable WAL coefficient $\alpha$ (maximum close to 3/2) from quantum transport experiments. Most importantly, it is identified that the spin-polarized surface electrons from dual topological bands exhibit circularly and linearly polarized photogalvanic effect (CPGE and LPGE). It is anticipated that the stacked dual-topology and stacking layer number controlled bands evolution provide a platform for realizing intrinsic CPGE and LPGE. The results show that the surface electronic structure of the dual TSLs is highly tunable and well-regulated for quantum transport and photoexcitation, which shed light on engineering for opto-electronic/spintronic applications.

## 1. Introduction

Topological insulators (TIs) possess metallic states with a linear dispersion relation on the boundary or surface which are protected by time-reversal symmetry (TRS) and characterized by a nonzero $Z_2$ invariant.[1] The spin and momentum of topological edge states (2D TIs) or surface states (3D TIs) are orthogonally locked and robust against nonmagnetic backscattering.[2] Beyond the $Z_2$-order protected band topology, the crystalline symmetry preserves the band topology in cases such as discrete rotation and mirror symmetry which defines the topological crystalline insulators (TCIs).[3] A combination of these two topological properties in one material, i.e., dual topology, defines a dual TI and offers fertile possibilities of gapping one topological surface state via breaking the respective symmetry while preserving another.[4] Therefore, the exploration of dual TIs can elucidate more degrees of freedom to manipulate the band structure and electric transport properties for designing novel topological electronic, spintronic, thermoelectric, and optical devices.[5]

Dual TIs can exist in different topological forms.[6] One form refers to dual protection of surface states by multiple bulk symmetries, such as $Bi_2Te_3$[6b] predicted to be both a TI and a TCI whose topological surface state is protected by TRS and crystal symmetry simultaneously. Another interesting form is that the dual TIs can

H.-p. Xue, R. Sun, X. Yang, J.-n. Liu, Y.-s. Wei, Q.-l. Yang, X.-s. Gai, Z.-z. Gong, Z.-k. Xie, N. Li, X.-q. Zhang, W. He, Z.-h. Cheng
Beijing National Laboratory for Condensed Matter Physics
Institute of Physics
Chinese Academy of Sciences
Beijing 100190, China
E-mail: zhcheng@iphy.ac.cn
H.-p. Xue, R. Sun, X. Yang, J.-n. Liu, Y.-s. Wei, Q.-l. Yang, X.-s. Gai, Z.-z. Gong, Z.-k. Xie, N. Li, Z.-h. Cheng
School of Physical Sciences
University of Chinese Academy of Sciences
Beijing 100049, China

R. Sun, A. Comstock, D. Sun
Organic and Carbon Electronics Lab (ORaCEL)
North Carolina State University
Raleigh, NC 27695, USA
E-mail: dsun4@ncsu.edu
Y. Liu, B. Ge
Information Materials and Intelligent Sensing Laboratory of Anhui Province
Institutes of Physical Science and Information Technology
Anhui University
Hefei 230601, China
Z.-h. Cheng
Songshan Lake Materials Laboratory
Dongguan, Guangdong 523808, China

be constructed via stacking 2D TIs layers with weak interlayer hybridization and mirror symmetry perpendicular to the construction direction,[4,6a,7] which has two surface states protected by TRS and mirror symmetry, respectively. There is except for the case that the band structure of heterojunction of 3D TI/2D TI, such as $Bi_2Te_3/Bi$[8] or $Bi_2Se_3/Bi$[9] is just the superposition of 2D Dirac cone states of TI and Bi, leading to a formation of additional Rashba states. One typical example is the layered compound $Bi_2TeI$ where the 2D TI layer Bi is sandwiched by two layers of a trivial semiconductor BiTeI to construct a weak TI.[7a,10] However, the time reversal and mirror symmetry-protected Dirac surface states of $Bi_2TeI$ reside in different facets assigned with weak topological indices and mirror Chern numbers. A similar example of such a dual topological system is $Bi_1Te_1$[4] consisting of double layers of 3D TI $Bi_2Te_3$ and one bilayer of Bi, whose weak TI and TCI states are not located on the same termination. The exhibition of dual topological surface states on different facets may limit the application of low-dimensional heterostructure devices. While only one single 3D strong TI layer $Bi_2Se_3$ is incorporated between 2D TI Bi, a TI surface state will inherit the bulk property of both topological layers, and the strong TI surface states (TISs) and TCI surface states (TCISs) can emerge on the same facet.[5b,11] It may become more applicable for multitopological state manipulation considering the correlation of facet, topology, and symmetry.[12] Until now, different topological classes of dual TIs have been demonstrated by ab initio density functional theory calculation, angle-resolved photoelectron emission spectroscopy (ARPES), and scanning tunneling spectroscopy.[4,5c,6a] However, the correlation of quantum transport with the electronic structure of a dual TI is not well understood yet, and their potential applications such as optoelectronics by utilizing dual TI states have also never been explored. Here, we constructed $Bi_2Se_3$-$(Bi_2/Bi_2Se_3)_N$ topological superlattices (TSLs, $N$ is the stacking layer number, when $N = \infty$ $Bi_4Se_3$ is predicted to be a dual TI[11]) consisting of alternating one bismuth bilayer (Bi BL) and one quintuple bismuth selenide layer ($Bi_2Se_3$ QL) via molecular beam epitaxy (MBE). Based on ARPES, we can identify the TISs and TCISs coexist in the $Bi_2Se_3$-terminated topological superlattices. As $N$ increases from 1 to 13, the Dirac point of TCI ($D_{TCI}$) and TI ($D_{TI}$) shifts from the estimated value $-0.25$ eV ($-0.8$ eV for $D_{TI}$) for $N = 1$ to $+0.1$ eV ($-0.5$ eV for $D_{TI}$) for $N = 13$ (about 0.3 eV), and $D_{TCI}$ approaches to Fermi level and finally crosses over the Fermi level at $N = 7$. From magnetoconductance (MC) measurements, we observe that the electron–electron interaction (EEI) and weak antilocalization effect (WAL) play an important role in the low-dimensional TSLs, and more coherent channels contribute to WAL when the Dirac point of TCI, $D_{TCI}$, located near Fermi level. Moreover, via low-energy photon excitation exploration, the stacking layer number $N$ regulated spin-polarized bands also lead to pronounced $N$-dependent circularly and linearly polarized photogalvanic effect (CPGE and LPGE), revealing the coherent entanglement of TCI and TI surface electrons. In contrast to CPGE originated from optical selection rules of the spin-split subbands, LPGE only emerges with coherent channels of TCI and TI intermixing states where asymmetric electron scattering occurs. Our observation of a dual TI band structure modulated quantum transport and optical excited photocurrent would give more insights of investigations of dual topological states with manifestation on one facet for electronic, spintronic, or optospintronic device application.

## 2. Formation of Dual TSLs and ARPES Measurements

**Figure 1**a shows a schematic diagram of TSLs with alternative stacking of 2D and 3D TIs. Along the stacking direction, one 2D TI Bi bilayer is sandwiched by two 3D TI $Bi_2Se_3$ quintuple layers. The small lattice mismatch between these two building blocks enables well-ordered crystalline samples and the infinite stack sequence of $(Bi_2Se_3/Bi_2)_N(N \to \infty)$ has a hexagonal layered structure with space group $R\bar{3}m$.[13] The comparable spin–orbit coupling (SOC) of these two blocks is inherited from the same element Bi and their weak covalent bonding strength enforces the progressive coupling of adjacent 2D and 3D TIs. Inside the dotted box (Figure 1a), it depicts the SOC of the electrons between the $Bi_2$ bilayer and the $Bi_2Se_3$ layer.[11] Generally speaking, when two different energy bands overlap with each other, the existence of their SOC opens an exchange gap.[11] In the $Z_2$ language, the exchange gap between surface states can be naturally obtained where the topological energy band crosses for the $(1 + 1)$ mod $2 = 0$.[14] However, when the stacked topological system preserves mirror symmetry for the plane along the surface normal M', a gapless surface state emerges due to the topological protection by a mirror Chern number, as described as a TCI in Figure 1b. Assuming that the topological properties of the parent layer $Bi_2Se_3$ are still preserved on the surfaces with SOC, the acquired TCI from mirror symmetry protection makes the stacked topological system a dual topological phase on the same facet. Fortunately, the Bi and $Bi_2Se_3$ layers share the same space group $R\bar{3}m$, and the three mirrors along $\Gamma - M$ perpendicular to the surface would be preserved throughout epitaxial growth. The dual topology can be classified from the band inversions located at the time-reversal invariant momentum (TRIM) $\bar{\Gamma}$ and along $\bar{\Gamma}-\bar{M}$ of the 2D surface Brillouin zone (Figure 1c). As a consequence, the surface state protected by TRS is still preserved at the $\bar{\Gamma}$ point accompanied with three pairs of Dirac surface states at non-TRIM points along $\bar{M}-\bar{\Gamma}-\bar{M}$ lines on (001) surface simultaneously. Figure 1d depicts the Fermi contour of $Bi_2Se_3$-TSL$_{N=5}$ with a clear hexagonally warped Fermi surface near the center of the first surface Brillouin zone, which is similar to 3D TI $Bi_2Se_3$. The energy–momentum ($E$–$k$) image along $\bar{M}-\bar{\Gamma}-\bar{M}$ in Figure 1e (left) remarkably shows two Dirac-like bands, with Fermi level $E_F = 0.0$ eV, one at the $\bar{\Gamma}$ point around $-0.7$ eV termed as $D_{TI}$ and the other on the mirror-invariant $\bar{\Gamma}-\bar{M}$ azimuth around $-0.1$ eV termed as $D_{TCI}$, which indicates the coexistence of different symmetry-protected topological surface states on the same facet. Corresponding momentum-dispersion curves (MDCs) in Figure 1e (middle) show a pronounced TI surface state, implying strong topological protection despite the Coulomb attractive interaction between the Bi and $Bi_2Se_3$ layers.[15] Figure 1e (right) shows the second derivative image of MDCs (2nd MDCs), which offers an enhanced resolution of the Dirac linear bands from TCI and TI states. The strong TI surface state in the reduced dimensional TSLs is similar to that
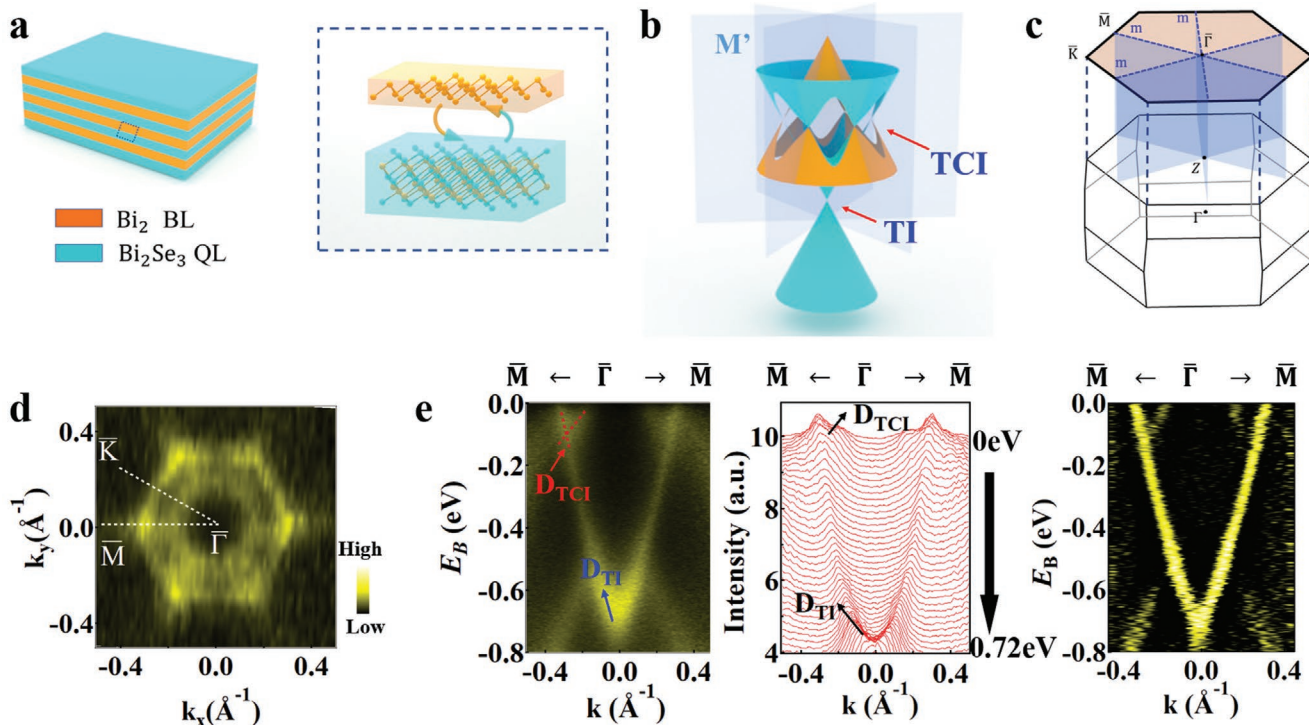
**Figure 1.** Formation mechanism and band characterization of dual topological surface states. a) Schematic diagram of complete TIs stacking structure with finite periods. The TSL is consisted of alternating $Bi_2Se_3$ quintuple layers (QLs) and Bi bilayers (BLs) structure (repeating periods, $N$) with $Bi_2Se_3$ termination. The dotted box shows the spin–orbit coupling of 2D electrons between QLs and BLs.[11] b) The schematic illustration of the formation of dual topological states. The spin–orbit coupling can induce an exchange gap where two Dirac cones overlap. With mirror symmetry protection, the gap will be closed, leading to six Dirac cones on the $Bi_2Se_3$ surface. Light blue planes M' represent the mirror planes. c) Bulk Brillouin zone and its 2D projection to (0001) surface, where blue planes represent three equivalent mirrors. d) The Fermi surface of $(Bi_2Se_3$-$Bi_2)_{N=5}$ from ARPES. e) From left to right, the $E$–$k$ curves, MDCs, and 2nd MDCs, measured along $\overline{M}-\overline{\Gamma}-\overline{M}$, clearly show the coexistence of TCI and TI states (denoted by $D_{TCI}$ and $D_{TI}$), which are almost identical to spin split bands from surface contribution.[5b]

in the previously reported bulk material $Bi_4Se_3$ with $D_{TI}$ located at 0.6 eV below the Fermi level.[16] However, the crossed TCI energy bands are less clear than the TI surface state. Nevertheless, it indicates the nontrivial property of topological protection in the stacked TSLs.

To further reveal the mirror-symmetry-protected band crossings at non-TRIM points, we performed systematic band analysis. **Figure 2**a depicts the experimental ARPES spectra along high-symmetry and non-high-symmetry lines in $k$-space which exhibit the topological crystalline character of the stacked TSLs. Compared to the ARPES spectra taken along high-symmetry lines $\overline{\Gamma}-\overline{M}$ with $\overline{\Gamma}-\overline{K}$ cut, there is a hybridization gap with an energy gap of about 0.10 eV along $\overline{\Gamma}-\overline{K}$ extracted from the energy distribution curve while no obvious gap along $\overline{\Gamma}-\overline{M}$ direction but a Dirac crossing point around −0.09 eV at $k \sim 0.25$ Å$^{-1}$. The Dirac point is derived from the existence of mirror symmetry protection which forbids the SOC gaps along $\overline{\Gamma}-\overline{M}$. By comparing our ARPES of a wide area of in-plane ordered samples with previous works,[5b] we can confirm the existence of dual topological surface states in low-dimensional topological superlattice on the $Bi_2Se_3$ facet. This feature indicates the consequence of the mirror-symmetry-protected Dirac surface state of the stacked TSLs.[11]

Stacking layer number $N$ usually significantly affects the electronic properties of conventional superlattices and 3D TIs,

e.g., quantum confinement effect,[17] which greatly modifies the band structure. Figure 2b shows a series of ARPES spectra of TSLs $(Bi_2Se_3/Bi_2)_N$ along $\overline{M}-\overline{\Gamma}-\overline{M}$ with various repeating period numbers $N = 1, 5, 7, 11, 13$. Clearly, with increasing $N$ from the ultrathin stacking layer ($N = 1$) to thick stacking layer ($N = 13$), the "V"-type TI surface state is still preserved. Interestingly, the position of the Dirac point $D_{TI}$ shifts from −0.8 eV for $N = 1$ to −0.5 eV for $N = 13$. The position of the Dirac point $D_{TI}$ of TSL $_{N=13}$ is similar to the 3D bulk $Bi_4Se_3$, which remarkably shows the magnificent effect of stacking layer number regulation. Simultaneously, the TCI Dirac point $D_{TCI}$ (marked with red crossed lines) is located at around −0.25 eV for the sample with $N = 1$, which is 0.15 eV deeper than that for the sample with $N = 5$. It overtakes the Fermi level when $N$ is above 7. **Figure 3**c shows the variation of the estimated energy distance of $D_{TI}$ and $D_{TCI}$ relative to the Fermi level as a function of $N$ (when $N > 7$, the position of $D_{TCI}$ is inferred with respect to $D_{TI}$ assuming the relative distance between $D_{TI}$ and $D_{TCI}$ keeps constant). In general, the overall electronic structure of dual TI on $Bi_2Se_3$ facet is less modulated by the stacking layer number, while the relative position of $D_{TI}$ and $D_{TCI}$ presents a monotonic up-shift of about 0.3 eV. This up-shift can be ascribed to the modulation of the charge transfer effect from electron donor Bi BL to electron acceptor $Bi_2Se_3$ QL.[15b]
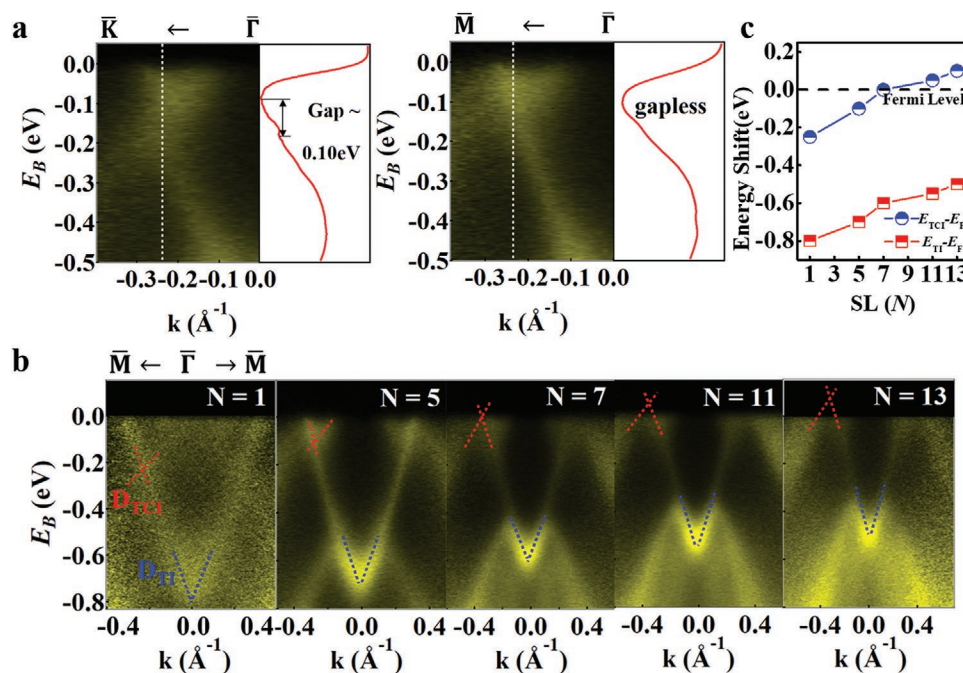
**ADVANCED**
**SCIENCE NEWS**

www.advancedsciencenews.com

**ADVANCED**
**MATERIALS**

www.advmat.de

**Figure 2.** Symmetry and stacked layer number-dependent band structure. a) The $E-k$ image and EDCs along $\overline{\Gamma}-\overline{M}$ with mirror symmetry and $\overline{\Gamma}-\overline{K}$ without mirror symmetry for $N = 5$. Obviously, the sub-band breaks off along $\overline{\Gamma}-\overline{K}$ with a gap of about 0.1 eV while it continues at the band crossing due to the mirror symmetry protection. b) ARPES spectra of energy dispersion at the Fermi surface of superlattices $Bi_2Se_3 - (Bi_2Se_3\text{-}Bi_2)_N$ with $N = 1$, 5, 7, 11, 13, respectively. The Dirac cone of TCI $D_{TCI}$ is marked with red crossing lines and the Dirac cone of TI $D_{TI}$ is marked with blue crossing lines. c) The estimated binding energy shift of $D_{TI}$ and $D_{TCI}$ as a function of TSLs' stacking layer number $N$.

## 2.1. Transport Properties of TSLs

To gain more deep insights into dual topology-modulated quantum transport properties, we performed low-temperature transport measurements. WAL,[18] a typical characteristic of surface states in topological materials, usually occurs at low temperatures and low magnetic fields, which originates from quantum interference (QI) between backscattered electrons when Dirac electrons acquire a $\pi$ Berry phase after circling on the spin-momentum-locked surface.[19] A series of $Bi_2Se_3$-TSLs samples were fabricated into a standard Hall bar geometry (Figure 3a). First, we performed magnetoresistance (MR) measurements with the magnetic field ($B$) at different tilting angle $\theta$, which allows us to distinguish the 2D WAL effect associated with the topological surface states from the 3D bulk effect. Figure 3b (take $Bi_2Se_3$-$TSL_{N=3,11}$ as examples, others seen in Figure S5, Supporting Information) shows MR as a function of the normal component of magnetic field $B$, i.e., $B\cos\theta$. When the magnetic field is parallel to the charge current direction ($\theta = 90°$, $B\|I$), the existence of a trivial parabolic MR curve indicates no contribution to WAL from 3D bulk-state-occupied electrons.[20] On the contrary, a visible negative MR dip occurs, a characteristic of WAL, when the magnetic field is perpendicular to the sample ($\theta = 0°$, $B\perp I$). It can be clearly seen that all the $R(\theta, B)$ curves nearly coincide with each other particularly in low magnetic fields. The angle-dependent magnetic field MR results demonstrate that the observed WAL is mainly derived from 2D surface states.[20,21]

According to 2D localization theory, magnetic field-induced suppression of WAL corrections in 2D systems is quantified by the Hilami–Larkin–Nagaoka (HLN) equation[22]

$$\Delta\sigma_{2D}(B) = \sigma_{2D}(B) - \sigma_{2D}(0) = -\frac{\alpha e^2}{2\pi^2\hbar}\left[\ln\left(\frac{\hbar}{4Bel_\phi^2}\right) - \Psi\left(\frac{1}{2} + \frac{\hbar}{4Bel_\phi^2}\right)\right]$$

(1)

which has been extensively applied to the surface states of topological materials.[18b,20,23] $\sigma$ is the sheet conductivity, $e$ is the charge of electron, $l_\phi$ is the phase coherence length which is the distance traveled by an electron before its phase is changed, $\alpha$ is the WAL coefficient representing the number of independent spin–orbit-coupled coherent transport channels (one spin-momentum-locked surface state contributes 1/2 at most),[24] and $\Psi$ is the digamma function, i.e., the logarithmic derivative of the gamma function. Figure 3c shows the MC and typical HLN fitting curves (up to 1T) at various temperatures for $N = 1$ (others seen in Figure S6, Supporting Information), from which the relationship between the phase coherence length $l_\phi$ and the temperature $T$ can be obtained. It can be noticed that the QI gets destroyed due to the randomization of phase at higher temperatures and nearly could not be observed above 50 K. We further fitted $l_\phi - T$ curves with $l_\phi \sim T^{-\gamma}$ shown in Figure 3d, where the index $\gamma = 0.33$, 0.5, 0.75 corresponds to an EEI dephasing mechanism in 1D, 2D, and 3D systems, respectively.[25] That the value of $\gamma$ is rough about 0.5 indicates the dephasing scattering mechanism mainly comes from a 2D system,[18a,26] which is consistent with WAL mainly originating from 2D surface states as mentioned above. Owing to the strong EEI in the reduced dimensional TI superlattice system (see Section S3, Supporting Information), the phase coherence length will be smaller compared to similar topological insulator materials.[18a,18b]

To characterize the SOC of the TSL system, we can introduce the term of spin–orbit scattering length ($l_{so}$) into the formula
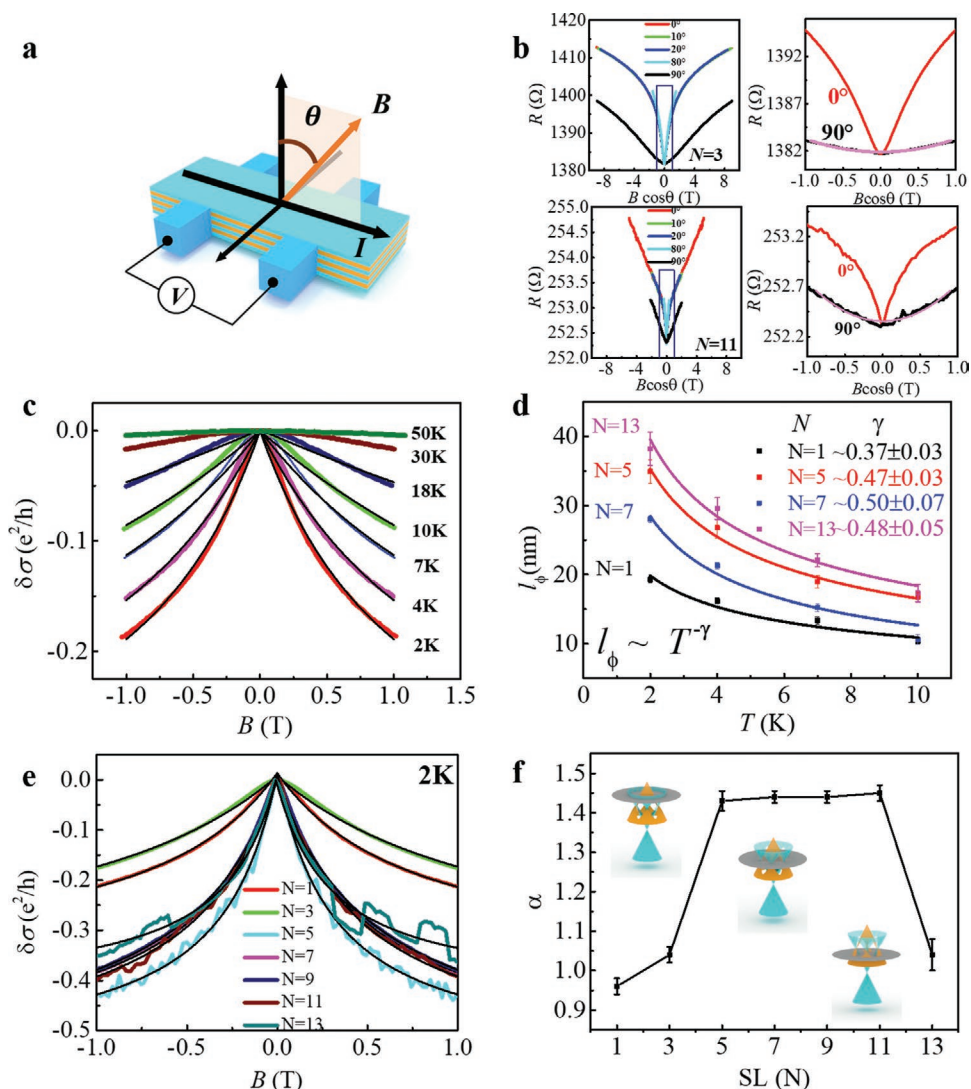
**Figure 3.** Temperature and stacked layer number-dependent WAL measurements of TSLs. a) Schematic view of transport measurements, where $\theta$ is the angle between the direction of the magnetic field and the normal direction of the sample surface. b) WAL measurements of different magnetic field inclinations of $N = 3$ and $N = 11$. The right panel shows MC at low fields (up to 1 T). When the magnetic field is perpendicular to the sample, it shows a typical cusp like WAL, and while the magnetic field is parallel to the sample, it shows a trivial parabolic form (with fitting). The inset picture shows the direction of the electric current and magnetic field, where $\theta$ is the angle between the direction of the magnetic field and the normal direction of the sample surface. c) The raw magnetic conductance data and HLN equation fitting of $(Bi_2Se_3\text{-}Bi_2)_{N=1}$ superlattices at different temperatures. d) The phase coherent length $l_\phi$ versus temperature curve and the fitting curve with $l_\phi \sim T^{-\gamma}$ in different superlattices. e) The raw magnetic conductance data and HLN equation fitting of different superlattices. f) The fitted $\alpha$ changes with the number of stacking layers $N$. Enhanced $\alpha$ is commonly associated with the helical spin texture of the topological Dirac dispersion. The insets show the corresponding changing trend of band structure evolution.

(formula 1 in Section S8, Supporting Information) to obtain $N$-dependent $l_{so}$ (Figure S8b, Supporting Information). No evident change of $l_\phi$ was observed after introducing spin–orbit scattering length $l_{so}$. We found that the $l_{SO}$ of TSLs does not change significantly with thickness. It is also in line with expectations, since the composition of our system has not changed. Furthermore, in Figure S3 in the Supporting Information, the conductance $\sigma(T)$ with different $B$ drops logarithmically with temperature for all the TSLs. The positive slope of $\sigma(T)$ can be denoted by $\kappa = \left(\dfrac{\pi h}{e^2}\right)\dfrac{\partial\sigma}{\partial\ln T}$, serving as additional evidence for the EEI. Figure 3e depicts the low-field (less than 1 T) MC-$\Delta\sigma$ of

$Bi_2Se_3$-TSLs ($N = 1, 3, 5, 7, 9, 11, 13$) at 2 K. The extracted WAL coefficient $\alpha$ from the HLN fit as a function of $N$ is shown in Figure 3f. Remarkably, as the $N$ increases, the value of $\alpha$, which represents the number of independent coherent channels, first increases and then decreases, varying from $\approx$1.0 to $\approx$1.5 and back to $\approx$1.0. The "terrace"-like trend is also evident when the background of linear MR is taken into account (Figure S7, Supporting Information) though $\alpha$ for $N = 11$ is greatly reduced.[27] It is worth noting that, in Figure S3 in the Supporting Information, $\delta\kappa$, a manifestation of the contribution of WAL to some extent, also has the "terrace"-like trend with $N$, which is consistent with $N$-dependent $\alpha$. The stacking layer $N$ dependence

of electron transport may be related to the regulation of electronic structure.

The nonmonotonic change of $\alpha$ indicates the contribution of additional QI channels. Comparing the quantum transport results with ARPES spectra in Figure 2, it can be concluded that the change of $\alpha$ originates mainly from the variation of the band structure near the Fermi level. As the $N$ varies, the position of $D_{TCI}$ relative to the Fermi level changes from $\approx -0.25$ to $\approx +0.10$ eV (estimated from Figure 2c). In the previous low-temperature transport study of 3D TI $Bi_2Se_3$, the $\alpha$ shows no evident thickness dependence for films thicker than 6 QL.[28] Such a nonmonotonic change of $\alpha$ cannot be ascribed to single topological surface state (TSS) contribution. Besides, the enhanced $\alpha$ emerging at $N = 5$–9 with value over 1.0 strongly demonstrates the pivotal role of TCISs in contributing to the transport channels. If there is only one TISs, the value of $\alpha$ will not change much and not exceed 1.0 in theory. Only when the Fermi level crosses the TISs and TCISs simultaneously can $\alpha$ exceed 1.0 (about 1.5) due to the additional contributions of the multiple TCISs. Such presumptions from the QI match quite well with ARPES results as shown in Figure 2b. Though the TCISs do play a vital role in QI transport, the contribution of TCISs is not as high as expected. According to the electronic band structure shown in Figure 1d, there are three pairs of TCISs around the Fermi level. Consequently, six extra equivalent channels to QI arise and cause the upper limit of $\alpha$ up to 7.0 (top and bottom surface). However, the observed $\alpha$ is largely reduced, which reflects the mutual scattering and coherent entanglement between Dirac cones from TCISs and TISs.[29,30] Usually, the WAL is contributed by the Dirac surface state with the same topology such as in a single TI or TCI system.[18b,30] The $N$-dependent WAL in the TSLs originates from a topological regulation by the topological states of the TSLs with dual topologies. In addition, the shift of the Fermi level with respect to the Dirac point is likely to alter the strength of the mutual scattering between the electrons on the surface of the Dirac cone. More detailed theoretical work may be needed to explore the mechanism behind it.

## 2.2. CPGE and LPGE Measurements of TSLs

In addition to the stacking layer number of TSLs dramatically affecting the band structure and low-temperature transport characteristics, it will also stir the surface electrons in a non-equilibrium process under light stimuli such as the CPGE and LPGE. CPGE is a unique probe to reveal topological surface states with spin-momentum locking,[31] which are forbidden from the contribution of bulk states with inversion symmetry in this case.[32] When the circularly polarized light is incident on the surface at an oblique angle $\theta$ (**Figure 4**a), based on the selection rules, only the spin-polarized electrons can be excited to unoccupied spin-polarized states resulting in the imbalance of carriers with opposite spin in $k$-space to generate a spin-polarized current. LPGE can arise from the asymmetric scattering of free carriers by phonons, static defects, or other carriers in noninversion symmetric systems,[33] and may be related to the origin of topological surface states.[31] So far, CPGE has been studied in strong SOC systems, such as 2D electron gas,[34]

Weyl semimetals,[35] topological insulators,[31,33,36] etc. With the coexistence of TCI and TI surface states on one facet in $N$-dependent TSLs, there may be interesting photogalvanic effects awaiting exploration.

Polarization-dependent photocurrent measurements were conducted as shown in Figure 4a. A diode laser with 1.17 eV was used and the light polarization was controlled by a quarter-wave plate (QWP). $\theta$ is the oblique angle between the light wave vector and the normal direction of the sample surface which is marked by the $z$-axis. The incident plane is set as a $y$–$z$ plane, and the electrode direction is along the $x$-axis. Figure 4b shows the measured photocurrent as a function of $\phi$ for $N = 9$, with $\theta = -45°$. The photocurrent can be fitted phenomenologically by the following formula[36c,37]

$$I = I_C \sin 2\phi + I_L \sin(4\phi - \varphi) + I_0 \qquad (2)$$

here $\phi$ is the angle of the slow axis of the QWP with respect to the emitted linearly polarized light. $I_C$ and $I_L$ represent the amplitude of the CPGE and LPGE currents, respectively. $\varphi$ is related to the angle between the coordinate axis $y$ and the crystallographic axis.[33] Both CPGE and LPGE current can be well-fitted by $I_C \propto \sin\theta$ ($\theta$ is the incident angle), vanishing at normal incidence as shown in Figure 4c.[38] Quite different from previous reports where a photo drag effect drives the photocurrent response,[33] the photocurrent from LPGE is predominantly present in TSLs with $N = 9$. Both CPGE and LPGE currents vary linearly with the light intensity as shown in Figure 4c inset, which is expected according to phenomenological and microscopic theories.

Compared with the ARPES and transport measurements above, the evolution of band structure exerts great influence on topological electron transport. Such influence might be the same on the photocurrent response. Figure 4e,f shows $I_C$ and $I_L$ as a function of $N$. According to previous band structure calculations and deep-energy band structure mapping,[5b,11,15b] we assume the CPGE current is carried by electron states near the Fermi level due to the absence of hole bands which satisfy the energy conservation law. When $N = 1$, the magnitude of $I_C$ is weak because when the TCI crossing point is well below the Fermi level, there are few spin-polarized electrons from topological states contributing to CPGE current under the optical selection rules according to the band structure in Figure 2b. As $N$ increases, the $D_{TCI}$ approaches the Fermi level and more electrons can be excited from bottom hole spin-polarized states to top electron spin-polarized states as shown in Figure 4d ($N = 5$). The circularly polarized light selectively excited the spin-polarized Dirac electrons above the Fermi level, giving rise to the asymmetric distribution of electrons. Consequently, the CPGE current increases obviously. When $D_{TCI}$ continues to approach the Fermi level, due to the decrease of state density from the forbidden exchange gap region and the spin degeneracy around Dirac point in Figure 2a,[11] $I_C$ would decrease but preserve a minimum at $N = 7$ shown in Figures 2a and 4d. When $N$ increases to 11 and 13, the Fermi level is located far below $D_{TCI}$, and as the energy band slope (Fermi velocity $\sim \Delta E/\Delta k$) decreases, the previously excited states no longer meet the photo-selection rules near Fermi level (Figure S9, Supporting Information), and $I_C$ becomes smaller. On the other hand, the

**ADVANCED
SCIENCE NEWS**

www.advancedsciencenews.com
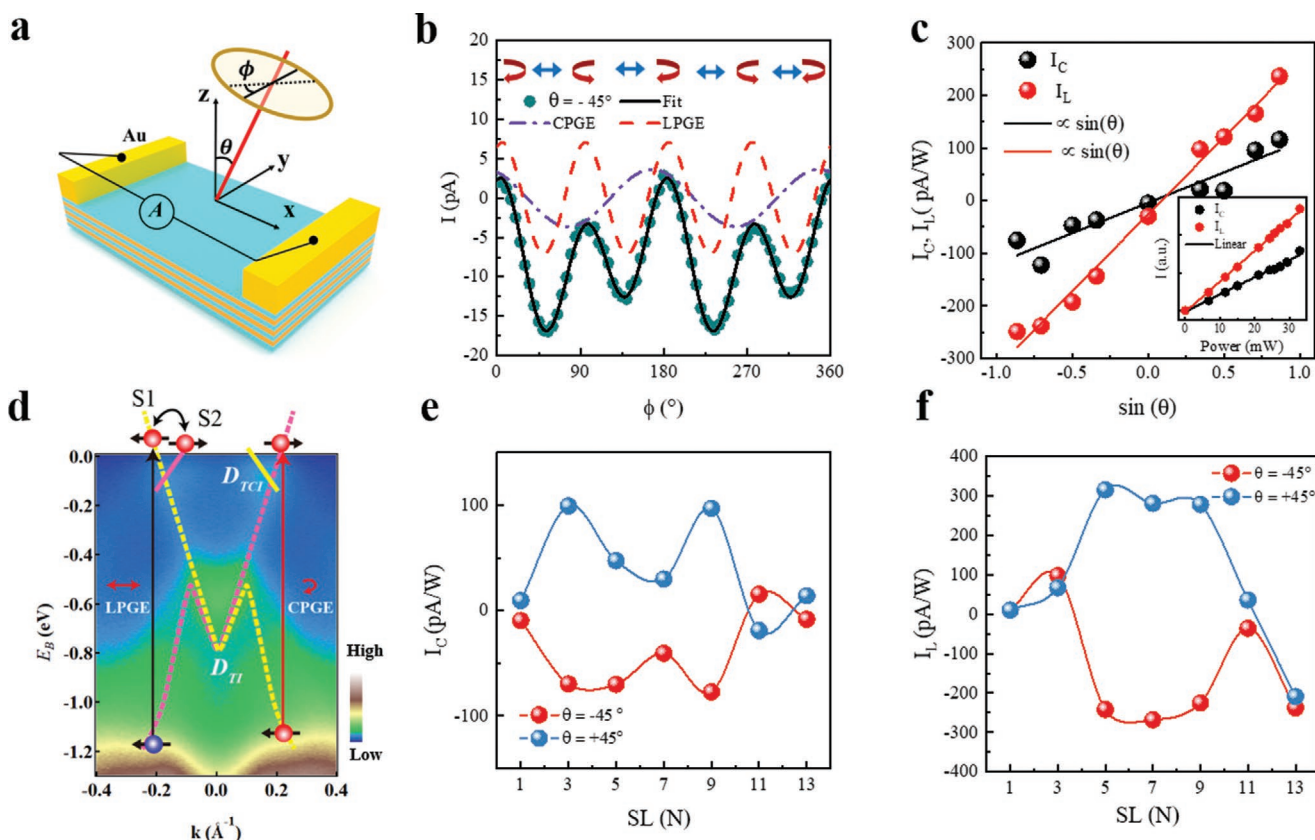
**ADVANCED
MATERIALS**

www.advmat.de

**Figure 4.** Stacked layer number-dependent CPGE measurements of TSLs. a) Schematic view of the photocurrent measurement setup. b) The photocurrent as a function of phase angle $\phi$ at an incident angle $\theta = -45°$. The black solid line represents the fitting curve according to Equation (2). c) The incident angle $\theta$ dependence of the CPGE current $I_C$ and LPGE current $I_L$. The inset shows the power dependence of $I_C$ and $I_L$ measured at $\theta = -45°$. All the solid lines are linearly fitted. d) Schematic illustration to explain the generation of CPGE and LPGE under polarized light illumination. The yellow and pink bands depict the spin-polarized surface states with opposite spin angular momentum from TI (dashed line) or TCI (solid line). The ARPES spectra show the band structure at $N = 7$. The electrons can be easily excited to the unoccupied surface states with opposite spin near the Fermi level, giving rise to large response of CPGE. Meanwhile, the LPGE occurs when the electrons are excited from low bulk states (blue electron) to high TI/TCI surface bands (red electron) with a scattering between subband S1 and subband S2. Consequently, a stronger LPGE current was observed when $D_{TCI}$ is located near Fermi level with a smaller momentum transfer. e,f) The dependence of CPGE and LPGE on stacking layer number $N$ at $\theta = -45°$ and $45°$, respectively.

thickness dependence of LPGE can exclude its origin from extrinsic contribution such as photoionizing defects,[39] but is tightly related to the evolution of the band structure. When $N = 1$, similar to CPGE, $I_L$ is small because of fewer excited states near the Fermi level. As $N$ approaches 7, the exchange coupled topological surface states may be excited under linearly polarized light when the TCI states approach the Fermi level (transition between light-blue band and conduction bands in Figure 4d). Unlike CPGE meeting spin selection rules, LPGE current occurs when bulk electrons are excited to subbands of TCI and TI surface states. It is noted that under the restriction of time reversal symmetry preservation, LPGE must be related to dissipative processes.[39a] As shown through quantum transport, there is mutual scattering and coherent coupling between TI and TCI surface states (S1 and S2, depicted in Figure 4d). It is possible that scattering between these two channels provides the ground for the generation of LPGE. Thus, the LPGE drops at $N = 11$ and even disappears at $N = 13$ with an even-symmetric $I_L$ respect to $\theta$ ($\theta = \pm 45°$) when the TCI states are far away from Fermi level. This explains why LPGE current has been barely

observed in topological insulators with a single Dirac cone, which presents a lack of optical transitions and scattering.[31,33] The observed pronounced LPGE and CPGE enable the dual topological system for the detection of light polarization but the involved physical process needs more comprehensive theoretical and experimental explorations.

## 3. Discussion

We constructed the low-dimensional complete topological superlattices $(Bi_2Se_3)$-$(Bi_2/Bi_2Se_3)_N$ ($N = 1, 3, 5, 7, 9, 11, 13$) with a selected facet via MBE. We verified the coexistence of TI and TCI surface states on the same facet of $Bi_2Se_3$ termination. TSLs exhibit a "V"-type TI state at the $\Gamma$ point due to strong topological $Z_2$ protection. Moreover, at the non-TRIM points along $\overline{\Gamma} - \overline{M}$ mirror plane direction, the gapless TCI surface states are preserved due to mirror symmetry protection. We also found the position of $D_{TI}$ and $D_{TCI}$ moves about 0.3 eV as $N$ increases which can ascribed to the charge transfer

effect from a confined charge rebalance process. Besides, the band information of TSLs is also evidenced by low-temperature transport results. Different from prototypical 3D TI transport behavior, the observed EEI and WAL effects are directly associated with the relative location between the Fermi level and TCI Dirac points. A pronounced enhancement of $\alpha$ appears with absolute value over 1.0 when $D_{TCI}$ approaches to Fermi level. The $N$-dependent WAL contributed by the dual topological states distinguishes these TSLs from other TI or TCI systems protected by a sole topology. At last, we show proof-of-concept control over photocurrent generation via dual topological modulation. The $N$-dependent CPGE and LPGE current varies with band structure and is tightly related to the position of $D_{TCI}$ and Fermi level. More importantly, the large nontrivial LPGE occurs, which is related to the mutual scattering between TI and TCI surface states. These features depict the nature of dual topological protection on one facet and imply the fabulous tunability of band structure via $N$ control of TSLs, which may give rise to giant modulation of spin transport and polarized optical excitation process.

To conclude, the dual topological system is established by stacking the 2D and 3D TI units. The band structures with coupled TI and TCI surface states near Fermi level evolved with $N$, directly influencing the electronic transport and nonequilibrium photoexcitation process. From a practical point of view, one can artificially design a series of dual topological materials to implement the property of TI and TCI simultaneously or separately for topological electronic, spintronic, and optic applications.

## 4. Experimental Section

*Sample Growth*: A series of natural topological superlattice $(Bi_2Se_3)$-$(Bi_2/Bi_2Se_3)_N$ ($N$ = 1, 3, 5, 7, 9, 11, 13) were grown via MBE on Si (111) substrate with the base pressure of $2 \times 10^{-10}$ mbar for ARPES measurements, or on $Al_2O_3$ (0001) substrate for transport measurements. For Si substrates, after pretreatment through a small current, it was heated by a stepwise increase of short-time DC current until the $7 \times 7$ surface reconstruction appeared in the low energy electron diffraction (LEED).[5b] Growth temperature and time were controlled with precision to avoid the reaction of Bi BLs with excess Se to form additional $Bi_2Se_3$ layers which would introduce miscellaneous phases. X-ray diffraction pattern conformed well to standard PDF cards (see Section S1, Supporting Information). Transmission electron microscope image (Section S1b, Supporting Information) showed that the prepared TSL had a crystalline structure grown along the [0001] direction where the atomic layers of Bi and Se were continuous and well-aligned at the atomic level in the absence of displacement of Bi and Se atoms. LEED and reflection high-energy electron diffraction of the samples grown on $Al_2O_3$ were also performed (Section S10, Supporting Information). The crystal structure of samples on $Al_2O_3$ substrate was the same as those of the samples grown on Si (Section S10, Supporting Information).

*ARPES Measurements*: An Se capping layer of 6 nm was grown on $Bi_2Se_3$ termination after the preparation of $Bi_2Se_3$-TSLs with various $N$ to prevent the surface state from being destroyed before measurements. Before transfer to the ARPES chamber to detect band structures of TSLs, the samples were first heated up to about 550 K and kept for 1.5 h to get rid of Se capper. ARPES measurements were performed at 4.5 K with the photon source of 21.2 eV from a He discharge lamp. Scienta DA30 was used to analyze electron energy. The energy and angular resolution were better than 20 meV and 0.5°, respectively. ARPES measurements of the samples grown on $Al_2O_3$ were also performed (Section S10, Supporting

Information), which were the same as those of the samples grown on Si (Section S10, Supporting Information).

*Transport Measurements*: The samples were patterned into standard six probe Hall bars with a scale of 310 μm/60 μm (length/width) through photolithography and etching. Transport measurements were performed by a Quantum Design physical property measurement system (PPMS). The temperature range was 2–300 K and the magnetic field could be applied up to 14 T. A DC current in the range of 1–10 μA was applied for resistive measurements. To suppress the effect of Joule heating, pulses of electric current with a width of 80 ms were adopted for measurements.

*Photocurrent Measurement*: The photocurrent measurements were conducted at room temperature. The polarized laser beam was modulated at 377 Hz by an optical chopper and then passed through a QWP. By rotating the QWP, the polarization could be tuned continuously from circularly polarized light to linearly polarized light. The beam was focused to a spot size of ≈200 μm between the gold electrodes. At last, the photocurrent was measured with a lock-in amplifier.

## Supporting Information

## Acknowledgements

## Conflict of Interest

The authors declare no conflict of interest.

## Data Availability Statement

The data that support the findings of this study are available from the corresponding author upon reasonable request.

## Keywords

[1] M. Z. Hasan, C. L. Kane, *Rev. Mod. Phys.* **2010**, *82*, 3045.
[2] D. Hsieh, Y. Xia, L. Wray, D. Qian, A. Pal, J. H. Dil, J. Osterwalder, F. Meier, G. Bihlmayer, C. L. Kane, Y. S. Hor, R. J. Cava, M. Z. Hasan, *Science* **2009**, *323*, 919.
[3] L. Fu, *Phys. Rev. Lett.* **2011**, *106*, 106802.
[4] M. Eschbach, M. Lanius, C. Niu, E. Mlynczak, P. Gospodaric, J. Kellner, P. Schuffelgen, M. Gehlmann, S. Doring, E. Neumann, M. Luysberg, G. Mussler, L. Plucinski, M. Morgenstern, D. Grutzmacher, G. Bihlmayer, S. Blugel, C. M. Schneider, *Nat. Commun.* **2017**, *8*, 14976.

[5] a) M. Samanta, K. Pal, U. V. Waghmare, K. Biswas, *Angew. Chem., Int. Ed. Engl.* **2020**, *59*, 4822; b) R. Sun, S. Yang, X. Yang, A. Kumar, E. Vetter, W. Xue, Y. Li, N. Li, Y. Li, S. Zhang, B. Ge, X. Q. Zhang, W. He, A. F. Kemper, D. Sun, Z. H. Cheng, *Adv. Mater.* **2020**, *32*, 2005315; c) B. Focassio, G. R. Schleder, A. Pezo, M. Costa, A. Fazzio, *Phys. Rev. B* **2020**, *102*, 045414; d) C. M. Acosta, A. Fazzio, *Phys. Rev. Lett.* **2019**, *122*, 036401; e) Y. Xiong, Y. Wang, R. Zhu, H. Xu, C. Wu, J. Chen, Y. Ma, Y. Liu, Y. Chen, K. Watanabe, *Sci. Adv.* **2022**, *8*, eabo0375.

[6] a) N. Avraham, A. Kumar Nayak, A. Steinbok, A. Norris, H. Fu, Y. Sun, Y. Qi, L. Pan, A. Isaeva, A. Zeugner, C. Felser, B. Yan, H. Beidenkopf, *Nat. Mater.* **2020**, *19*, 610; b) T. Rauch, M. Flieger, J. Henk, I. Mertig, A. Ernst, *Phys. Rev. Lett.* **2014**, *112*, 016802.

[7] a) I. P. Rusinov, T. V. Menshchikova, A. Isaeva, S. V. Eremeev, Y. M. Koroteev, M. G. Vergniory, P. M. Echenique, E. V. Chulkov, *Sci. Rep.* **2016**, *6*, 20734; b) I. Belopolski, S.-Y. Xu, N. Koirala, C. Liu, G. Bian, V. N. Strocov, G. Chang, M. Neupane, N. Alidoust, D. Sanchez, H. Zheng, M. Brahlek, V. Rogalev, T. Kim, N. C. Plumb, C. Chen, F. Bertran, P. Le Fèvre, A. Taleb-Ibrahimi, M.-C. Asensio, M. Shi, H. Lin, M. Hoesch, S. Oh, M. Z. Hasan, *Sci. Adv.* **2017**, *3*, e1501692.

[8] T. Hirahara, G. Bihlmayer, Y. Sakamoto, M. Yamada, H. Miyazaki, S. Kimura, S. Blugel, S. Hasegawa, *Phys. Rev. Lett.* **2011**, *107*, 166801.

[9] R. Sun, S. Yang, X. Yang, E. Vetter, D. Sun, N. Li, L. Su, Y. Li, Y. Li, Z. Z. Gong, Z. K. Xie, K. Y. Hou, Q. Gul, W. He, X. Q. Zhang, Z. H. Cheng, *Nano Lett.* **2019**, *19*, 4420.

[10] P. Tang, B. Yan, W. Cao, S.-C. Wu, C. Felser, W. Duan, *Phys. Rev. B* **2014**, *89*, 041409.

[11] A. P. Weber, Q. D. Gibson, H. Ji, A. N. Caruso, A. V. Fedorov, R. J. Cava, T. Valla, *Phys. Rev. Lett.* **2015**, *114*, 256401.

[12] Y. Tanaka, T. Zhang, M. Uwaha, S. Murakami, *Phys. Rev. Lett.* **2022**, *129*, 046802.

[13] H. Okamoto, *J. Phase Equilib.* **1994**, *15*, 195.

[14] S. Murakami, in *Topological Insulators: Fundamentals and Perspectives* (Eds: F. Ortmann, S. Roche, S. O. Valenzuela), Wiley-VCH, Weinheim, Germany **2015**, pp. 11–30.

[15] a) M. Eschbach, M. Lanius, C. Niu, E. Młyńczak, P. Gospodarič, J. Kellner, P. Schüffelgen, M. Gehlmann, S. Döring, E. Neumann, M. Luysberg, G. Mussler, L. Plucinski, M. Morgenstern, D. Grützmacher, G. Bihlmayer, S. Blügel, C. M. Schneider, *Nat. Commun.* **2017**, *8*, 14976; b) J. Zhang, X. Liu, G. Huang, *Phys. Status Solidi B* **2015**, *252*, 2090.

[16] Q. D. Gibson, L. M. Schoop, A. P. Weber, H. Ji, S. Nadj-Perge, I. K. Drozdov, H. Beidenkopf, J. T. Sadowski, A. Fedorov, A. Yazdani, T. Valla, R. J. Cava, *Phys. Rev. B* **2013**, *88*, 081108.

[17] a) W. Liu, Z. F. Wang, Q. W. Shi, J. Yang, F. Liu, *Phys. Rev. B* **2009**, *80*, 233405; b) M. Fox, R. Ispasoiu, in *Springer Handbook of Electronic and Photonic Materials*, (Eds: S. Kasap, P. Capper), Springer International Publishing, Cham **2017**; c) Y. Zhang, K. He, C.-Z. Chang, C.-L. Song, L.-L. Wang, X. Chen, J.-F. Jia, Z. Fang, X. Dai, W.-Y. Shan, S.-Q. Shen, Q. Niu, X.-L. Qi, S.-C. Zhang, X.-C. Ma, Q.-K. Xue, *Nat. Phys.* **2010**, *6*, 584.

[18] a) J. G. Checkelsky, Y. S. Hor, R. J. Cava, N. P. Ong, *Phys. Rev. Lett.* **2011**, *106*, 196801; b) J. Chen, H. J. Qin, F. Yang, J. Liu, T. Guan, F. M. Qu, G. H. Zhang, J. R. Shi, X. C. Xie, C. L. Yang, K. H. Wu, Y. Q. Li, L. Lu, *Phys. Rev. Lett.* **2010**, *105*, 176602; c) M. Liu, J. Zhang, C. Z. Chang, Z. Zhang, X. Feng, K. Li, K. He, L. L. Wang, X. Chen, X. Dai, Z. Fang, Q. K. Xue, X. Ma, Y. Wang, *Phys. Rev. Lett.* **2012**, *108*, 036805.

[19] a) S.-Q. Shen, *Phys. Rev. B* **2004**, *70*, 081311; b) Y. Xia, D. Qian, D. Hsieh, L. Wray, A. Pal, H. Lin, A. Bansil, D. Grauer, Y. S. Hor, R. J. Cava, M. Z. Hasan, *Nat. Phys.* **2009**, *5*, 398.

[20] H. T. He, G. Wang, T. Zhang, I. K. Sou, G. K. Wong, J. N. Wang, H. Z. Lu, S. Q. Shen, F. C. Zhang, *Phys. Rev. Lett.* **2011**, *106*, 166805.

[21] a) H. Li, H. W. Wang, Y. Li, H. Zhang, S. Zhang, X. C. Pan, B. Jia, F. Song, J. Wang, *Nano Lett.* **2019**, *19*, 2450; b) J. J. Cha, D. Kong, S. S. Hong, J. G. Analytis, K. Lai, Y. Cui, *Nano Lett.* **2012**, *12*, 1107.

[22] S. Hikami, A. I. Larkin, Y. Nagaoka, *Prog. Theor. Phys.* **1980**, *63*, 707.

[23] a) S.-P. Chiu, J.-J. Lin, *Phys. Rev. B* **2013**, *87*, 035122; b) H. Wang, H. Liu, C. Z. Chang, H. Zuo, Y. Zhao, Y. Sun, Z. Xia, K. He, X. Ma, X. C. Xie, Q. K. Xue, J. Wang, *Sci. Rep.* **2014**, *4*, 5817; c) Y. Zhao, H. Liu, X. Guo, Y. Jiang, Y. Sun, H. Wang, Y. Wang, H. D. Li, M. H. Xie, X. C. Xie, J. Wang, *Nano Lett.* **2014**, *14*, 5244.

[24] H. Z. Lu, J. Shi, S. Q. Shen, *Phys. Rev. Lett.* **2011**, *107*, 076801.

[25] J. J. Lin, J. P. Bird, *J. Phys.: Condens. Matter* **2002**, *14*, R501.

[26] P. A. Lee, A. D. Stone, H. Fukuyama, *Phys. Rev. B: Condens. Matter Mater. Phys.* **1987**, *35*, 1039.

[27] Z. Wang, L. Yang, X. Zhao, Z. Zhang, X. P. A. Gao, *Nano Res.* **2015**, *8*, 2963.

[28] N. Bansal, Y. S. Kim, M. Brahlek, E. Edrey, S. Oh, *Phys. Rev. Lett.* **2012**, *109*, 116804.

[29] R. Akiyama, K. Fujisawa, T. Yamaguchi, R. Ishikawa, S. Kuroda, *Nano Res.* **2015**, *9*, 490.

[30] B. A. Assaf, F. Katmis, P. Wei, B. Satpati, Z. Zhang, S. P. Bennett, V. G. Harris, J. S. Moodera, D. Heiman, *Appl. Phys. Lett.* **2014**, *105*, 102108.

[31] J. W. McIver, D. Hsieh, H. Steinberg, P. Jarillo-Herrero, N. Gedik, *Nat. Nanotechnol.* **2011**, *7*, 96.

[32] P. Hosur, *Phys. Rev. B* **2011**, *83*, 035309.

[33] Y. M. Wang, J. L. Yu, X. L. Zeng, Y. H. Chen, Y. Liu, S. Y. Cheng, Y. F. Lai, C. M. Yin, K. He, Q. K. Xue, *J. Phys.: Condens. Matter* **2019**, *31*, 415702.

[34] S. Wang, H. Zhang, J. Zhang, S. Li, D. Luo, J. Wang, K. Jin, J. Sun, *Phys. Rev. Lett.* **2022**, *128*, 187401.

[35] F. de Juan, A. G. Grushin, T. Morimoto, J. E. Moore, *Nat. Commun.* **2017**, *8*, 15995.

[36] a) Y. Q. Huang, Y. X. Song, S. M. Wang, I. A. Buyanova, W. M. Chen, *Nat. Commun.* **2017**, *8*, 15401; b) K. N. Okada, N. Ogawa, R. Yoshimi, A. Tsukazaki, K. S. Takahashi, M. Kawasaki, Y. Tokura, *Phys. Rev. B* **2016**, *93*, 081403; c) P. Olbrich, L. E. Golub, T. Herrmann, S. N. Danilov, H. Plank, V. V. Bel'kov, G. Mussler, C. Weyrich, C. M. Schneider, J. Kampmeier, D. Grutzmacher, L. Plucinski, M. Eschbach, S. D. Ganichev, *Phys. Rev. Lett.* **2014**, *113*, 096601; d) Y. Yan, Z. M. Liao, X. Ke, G. Van Tendeloo, Q. Wang, D. Sun, W. Yao, S. Zhou, L. Zhang, H. C. Wu, D. P. Yu, *Nano Lett.* **2014**, *14*, 4389.

[37] a) J. Li, P. M. Haney, *Appl. Phys. Lett.* **2016**, *109*, 193903; b) L. Zhu, Y. Zhang, P. Lin, Y. Wang, L. Yang, L. Chen, L. Wang, B. Chen, Z. L. Wang, *ACS Nano* **2018**, *12*, 1811.

[38] S. N. Danilov, L. E. Golub, T. Mayer, A. Beer, S. Binder, E. Mönch, J. Minár, M. Kronseder, C. H. Back, D. Bougeard, S. D. Ganichev, *Phys. Rev. Appl.* **2021**, *16*, 064030.

[39] a) G. E. Pikus, E. L. Ivchenko, in *Narrow Gap Semiconductors Physics and Applications*, (Ed: W. Zawadzki), Springer, Berlin, Heidelberg **1980**, pp. 388–406; b) V. I. Belinicher, B. I. Sturman, *Sov. Phys. Usp.* **1980**, *23*, 199.